Article

Not peer-reviewed version

Synthesis of Ni@SiC/CNFs Composite and Its Microwave Induced Catalytic Activity

Haibo Ouyang *, Jiaqi Liu , Cuiyan Li , Leer Bao , Tianzhan Shen , Yanlei Li

Posted Date: 4 July 2024

doi: 10.20944/preprints202407.0347.v1

Keywords: Double shell catalyst; Electrospinning; Microwave irradiation; Degradation; active species; plasma

Article

Synthesis of Ni@SiC/CNFs composite and its Microwave Induced Catalytic Activity

Haibo Ouyang *, Jiaqi Liu, Cuiyan Li, Leer Bao, Tianzhan Shen, and Yanlei Li

Key Laboratory for Green Manufacturing & Functional Application of Inorganic Materials, School of Materials Science and Engineering, Shaanxi University of Science and Technology, Xi'an 710021, China

* Correspondence: ouyanghb@sust.edu.cn

Abstract: In this paper, a novel microwave catalyst Ni@SiC/CNFs (NSC), C/Ni (NC), and C/SiC (SC) were successfully synthesized by electrostatic spinning method, and proved to degrade methylene blue with high efficiency under microwave irradiation. The results imply that the catalyst Ni@SiC/CNFs with double shell structure gave a 99.99 % removal rate in 90 s for the degradation of methylene blue under microwave irradiation, outperformed the C/Ni and C/SiC and most other reported catalysts in similar studies. On the one hand, the possible mechanism of the methylene blue degradation should be ascribed to that double shell structure increases the polarization source of the material, resulting in excellent microwave absorption properties; and on the other, the in-situ generation of active species OH• and O_2 - under microwave radiation and the synergistic coupling effect of metal plasma greatly improved the degradation efficiency of methylene blue. The findings of this study could provide a valuable reference for the green degradation of industrial dye wastewater and its sustainable development process.

Keywords: Double shell catalyst; Electrospinning; Microwave irradiation; Degradation; active species; plasma

1. Introduction

With the rapid development of the economy and the increasing growth of population, the quantity of wastewater produced and its overall pollution load is continuously increasing worldwide [1–3]. According to the reports from the United Nations World Water Development, over 80 percent of wastewater worldwide is released into the environment without treatment. The releasing untreated or inadequately treated wastewater not only leads to harmful effects on human health but also results in negative environmental impacts and adverse repercussions on economic activities [4,5]. Water contamination caused by dye industries has caused more and more attention since the dyes are widely employed in various industries (e.g. textile, pharmaceutical, food, cosmetics, plastics, photographic, and paper industries) and possess a significant source of pollution [6–8].

Currently, various methods such as adsorption, coagulation, advanced oxidation, and membrane separation are used in the removal of dyes from wastewater [9,10]. In recent years, advanced oxidation processes (AOPs) have made remarkable progress in the field of wastewater treatment [11]. The degradation of dyes by AOPs contributes to the in-situ generation of free radicals with high oxidizing activity (·OH, O_2^-, SO_4^-·) [12]. These free radicals non-selectively react with most organics, being able to degrade even highly recalcitrant compounds and leading to extensive degradation or mineralization of contaminants [13,14].

Driven by the intense desire for lower cost, higher efficiency and facile procedure of advanced oxidation processes, electrochemical, plasma, electron beam, ultrasound, or microwave-based AOPs draws great attention in the area of wastewater treatment [15]. Among these evaluated AOPs, microwave-enhanced AOPs can greatly improve the degradation rate and shorten the reaction time, since the ability to induce a hot spot effect, plasma discharge effect, and photoelectric effect in the microwave field. (i) The hot spots are a micro-plasma region on the catalyst surface where

 doi:10.20944/preprints202407.0347.v1

temperatures can reach over 1200 °C, promoting faster production of active species and oxidation of organic matter [16]. Qi et al., Hu et al., Garcia-Costa et al., Lei et al., and Shen et al. utilized the microwave hot spot effect to efficiently degrade different organic pollutants [17–21]. (ii) When microwaves act on some protrusions or metals with special shapes and sizes, charges are accumulated at the protrusions, the nearby field is stronger than the air field, and plasma discharge occurs [22]. Qian et al, Zhao et al, Xu et al, and Zhang et al. used the plasma discharge effect generated under microwave for efficient treatment of refractory organic matter as well as white pollution [22–25]. (iii) Catalysts with semiconductor properties (e.g., transition metal oxides, semiconductors, and ferromagnetic metals) produce holes (h^+) and electrons (e^-) under MW excitation, and the excited h^+ and e^- may migrate to the catalyst surface and participate in redox reactions [17,26,27].

The catalytic properties of many materials can be induced by MW irradiation. When MW irradiates these materials, the interactions between them can heat the materials rapidly to generate active sites after absorbing and converting MW energy. Thus, it is a critical issue to develop microwave active catalysts with strong microwave absorption ability and efficient microwave energy transfer ability [28–30]. Nano-carbon materials have abundant void structures, which can increase the electron transmission path, improve conductive loss, and have a high specific surface area. At the same time, the inhomogeneous structure of the phase boundary generates abundant interfacial polarization and multiple relaxation, which enhances microwave attenuation and has great potential for practical applications [31]. Chen et al. prepared graphene micro-flowers with a diameter of about 2-5 μm by a three-step process. The results show that the graphene micro-flowers prepared by this method have low reflection loss and exhibit ideal microwave absorption characteristics [32].

However, due to poor impedance matching and single dielectric loss, the microwave absorption performance of carbon materials is not very ideal [33]. To gain an ideal microwave absorption catalyst, it is necessary to design the composition and structure of the single-phase carbon material reasonably. The ideal magnetic loss can be obtained by combining carbon material with magnetic material to induce magnetic properties, and the loss mechanism is enriched while the impedance matching is improved, the microwave absorption performance of the material can be significantly improved [34]. Magnetic materials (such as Fe, Co, Ni, and corresponding alloys) are a kind of ideal complementary materials because of their higher permeability, saturation magnetization, and snoek limit [35–37]. When the microwave irradiates the metal, a unique discharge phenomenon occurs, which can realize the coupling of the thermal effect and the plasma effect. Li [33] et al. synthesized the rod-like Ni@C composite and tested its microwave absorption properties. The results show that the rod-like Ni@C composite has good microwave absorption and high reuse efficiency. SiC is an ideal microwave absorber because of its high microwave absorption characteristics in the gigahertz frequency. The superior thermal conductivity means it can still be used as a catalyst carrier at high temperatures, thus ensuring high catalytic performance. However, due to its inherent low conductivity and single polarization characteristics, SiC needs to be combined with different magnetic materials or carbon-based materials to enhance electrical conductivity and enrich its polarization types to improve microwave absorption performance [38]. Samarjit Singh et al. prepared a Ni/SiC/ graphene composite material with a minimum reflection loss of -59.15dB, showing good microwave absorption performance [39].

Based on the above ideas, we propose a novel Ni@SiC/CNFs catalyst for MW-AOP. Except for the outstanding microwave absorption performance, carbon fibers, as supporting materials, possess high electron mobility and can boost charge separation/electron transfer and improve catalytic oxidation. When SiC and Ni nanoparticles can produce hole electron pair and strong plasma discharge under microwave irradiation. Holes electronic react with O_2 and H_2O in the air will produce a strong oxidizing active group. Hot spots and plasmas arising from this discharge phenomenon can reduce the chemical reaction times of contaminants present on the material and increase their degradation rates.

In this work, the Ni@SiC/CNFs composites as MV-AOP catalysts were synthesized by the electrostatic spinning method. The morphology, microstructure, and phase composition of the Ni@SiC/CNFs were characterized through complementary analytical ways. The microwave catalytic

 doi:10.20944/preprints202407.0347.v1

performance of Ni@SiC/CNFs was evaluated with MB as the target containment. The catalytic mechanism was proposed to explain the synergistic effect of Ni@SiC/CNFs catalyst under microwave irradiation.

2. Materials and Methods

2.1. Synthesis of Ni@SiC/CNFs

Ni@SiC/CNFs composites are prepared by electrostatic spinning combined with high-temperature carbonization. First of all, the precursor solution containing 10 mL of N, N-Dimethylformamide (DMF), 1.0 g of polyvinylpyrrolidone (PAN), 0.16g of polycarbosilane (PCS), 1.7 mol of ($Ni(CH_3COO)_2$), and 2 mol of thiourea was electrospun into a polymer fiber membrane. To maintain fiber morphology, the as-spun polymer nanofibers were subsequently presintered at 280 °C for 2 hours in the air followed by further carbonization at 1400 °C for 1 hour under Ar atmosphere. Finally, Ni@SiC/CNFs (NSC) composites were obtained. By changing the content of PCS(0g) in the precursor solution, C/Ni (NC) composite material was prepared. Changing the content of ($Ni(CH_3COO)_2$) (0mol)and thiourea(0mol) in the precursor solution, C/SiC (SC) composite material was prepared. Figure 1 is the schematic diagram of the preparation of different composite materials.

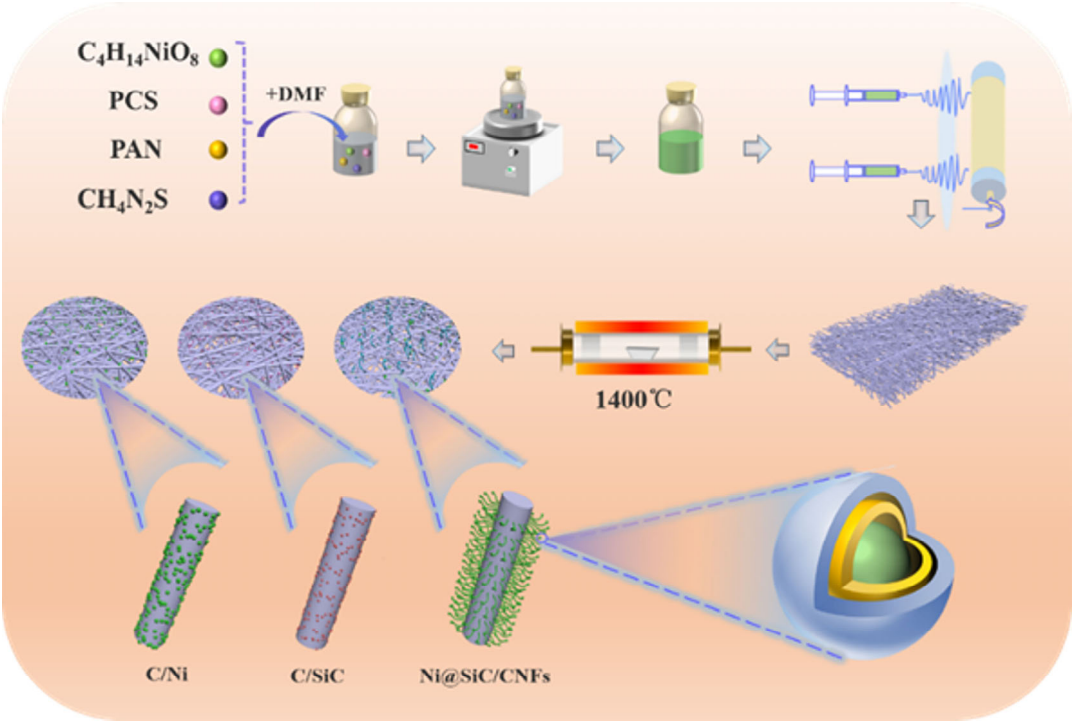

Figure 1. The flow diagram of preparing Ni@SiC/CNFs、C/Ni and C/SiC composites.

2.2. Characterization

The crystal structure of the sample was investigated using a powder X-ray diffractometer (XRD, Rigaku D/max-2200PC) with Cu Kα (λ= 0.15418 nm) radiation.

The morphology of the samples was observed using a field-emission scanning electron microscope (Hitachi, FE-SEM, S-4800).

XPS can be used for qualitative and quantitative analysis of the elements contained in the sample, and can also characterize the surface composition and chemical state of the sample.

High-resolution transmission electron microscopy (HRTEM) combined with energy dispersive spectroscopy (EDS) observation was performed on a FEI Tecnai G2 F20S-TWIN system at 200 kV.

 doi:10.20944/preprints202407.0347.v1

The UV-vis absorption spectra of the degraded were recorded on a UV/vis/NI R Spectrophotometer (LAMBDA950, PerkinElmer).

The dielectric property and magnetic permeability of the catalysts were analyzed by a vector network analyzer (Agilent 85071 E, USA).

2.3. Degradation experiment using microwave

To examine the catalytic activity of catalytic, degradation experiments were carried out using a controllable MW oven (WD750B, Galanz Company, China) equipped with a self-made glass reactor and a condensing tube. The specific operation is as follows: 20 mL of the MB solution and 20 mg of catalyst were added in a 50 mL

Teflon reaction vessel followed by microwave irradiation (450 W, 2450 MHz). Upon the desired reaction time, the mixture was cooled to room temperature. The reaction mixture was then analyzed to evaluate the degradation efficiency by an ultraviolet spectro-photometer (UV–vis, UV-2450, SHIMADZU, Japan). The removal rate of MB is calculated using the following formula:

$$Removal\ rate\ (\%) = \frac{C_0 - C_t}{C_0} \times 100\%$$

C_0 and C_t are the initial concentration and concentration after treatment time t of MB solution, respectively. Figure S1 is a schematic diagram of a microwave-assisted catalytic reactor.

3. Results

3.1. Microstructure and morphology

As depicted in Figure 2a, the NSC catalyst shows three clear and sharp diffraction peaks at 2θ=26°, 35.6°, and 45.5°, corresponding to (002) crystal plane of C, (111) crystal plane of SiC and (121) crystal plane of Ni, respectively. NC and SC catalysts only have the carbon diffraction peak and the corresponding Ni diffraction peak and SiC diffraction peak. Compared with the NSC catalyst, the diffraction peak intensity of SC catalyst SiC is much lower, which may be related to the addition of Ni particles. In addition, the SC catalyst corresponds to the mantou peak of carbon at 2θ=26°, while NC and NSC both show a sharp diffraction peak of C, indicating that Ni particles play a major role in the catalytic graphitization of composites at high temperatures. To prove the above conjecture, the graphitization of carbon was further confirmed using Raman spectroscopy (Figure 2b). Clearly, two typical carbon peaks at 1345 cm^{-1} and 1592 cm^{-1} were observed, corresponding to the D band and G band of carbon [40]. It can be found that the R value (ID/IG) of SC was the highest at 0.924, while that of NSC was the lowest at 0.754(Figure 2c), showing an obvious downward trend. It is well known that the D-band reflects the structural defects and disorder of carbon, while the G-band is related to graphitic carbon [41]. Therefore, a higher R value indicates more lattice defects of the C atom and a higher graphitization degree on the contrary. Herein the SC has the lowest graphitization, and the NSC has the highest graphitization, which corresponds to the XRD results. Materials with high graphitization have a higher dielectric loss, so their microwave absorption is increased [42].

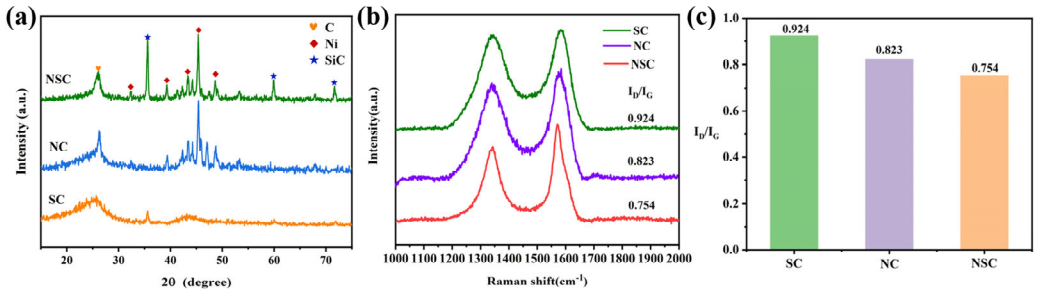

Figure 2. (a) XRD patterns; (b) Raman spectra; and (c) ID/IG graph of all the samples.

 doi:10.20944/preprints202407.0347.v1

The chemical compositions and surface states of the NSC were analyzed by XPS. The XPS full-survey scan spectrum of NSC shown in Figure 3a confirms C, O, Si, and Ni elements. The low strength of the Ni element may be because most of the Ni particles on the surface are coated with C. Figure 3b reveals the high-resolution C 1s spectra, which are deconvoluted into three stripping peaks, where 283.5, 284.6, 285.8 eV can be indexed to the C-Si, C-C, C-O peaks, respectively [43,44]. The Si 2p peak can be fitted into three peaks with typical binding energy of 101.4 and 103.4 eV, which are aligned with the Si-C bond and Si-O bond [45,46], respectively. Furthermore, the peak with a binding energy of 864 eV is attributed to Ni 2P, the peaks at 853.1 eV and 873.2 eV are assigned to Ni 2p3/2 and Ni 2p1/2 [47], respectively. Furthermore, the survey spectra of NC and SC are shown in Figure S2. The XPS results corresponded to the XRD analysis, which proved that the three catalyst materials were successfully synthesized.

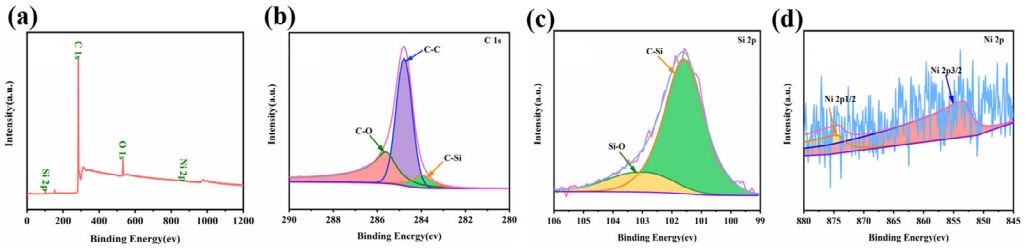

Figure 3. (a) XPS full spectrum; (b) XPS high-resolution spectrum of C1s; (c) Si 2p and (d) Ni 2p for the NSC composite materials.

The morphology of the sample was investigated using SEM. The microscopic morphology of the NSC catalyst is revealed by the scanning electron microscopy (SEM) image shown in Figure 4(a-d). SEM of NC and SC samples are shown in Figures S3 and S4 in Supplementary Materials. These nanofibers are highly interconnected with random orientations to form 3D continuous networked structures with excellent mechanical stability [48]. It can be seen from Figure 4a that plenty of nanowires with high flexibility are rooted from the surface of the carbon nanofibers, generating the 1D hierarchical architectures. Such a microscopic level network not only enhanced mechanical connection between fibers but also promoted electron transport and multiple reflections of microwaves in the network, which could benefit the dielectric properties of the hybrid fibers [31].

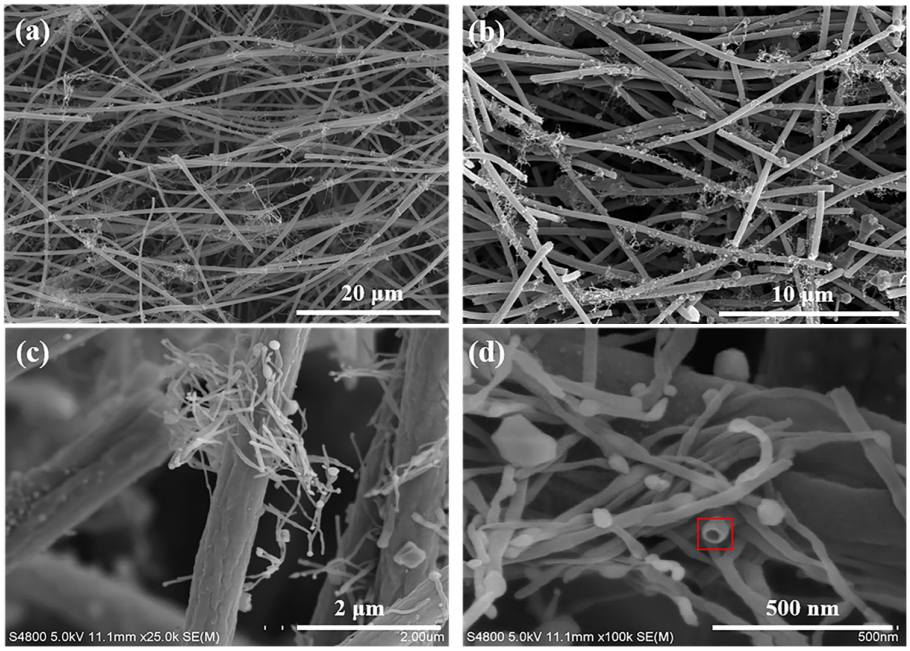

Figure 4. (a-d) SEM images of NSC catalyst at different magnifications.

 doi:10.20944/preprints202407.0347.v1

TEM and HRTEM analyses were performed to characterize the microstructure in more detail (Figure 5a-h). It is not difficult to see that Ni particles are covered and carbon nanotubes with a diameter of 15 nm grow from the surface of the cover layer, which is caused by Ni nanoparticles catalyzing the graphitization of amorphous carbon at high temperatures [49–51]. Surprisingly, a thin layer of SiC was precipitated on the surface of Ni particles, followed by a graphite carbon layer in the high-resolution HRTEM image in Figure 5d. This is mainly due to C and Si into the molten nickel particles at high temperatures. Due to the different precipitation temperatures of C and SiC, C is preferentially precipitated at low temperatures while SiC is precipitated after nucleation at a high temperature of 1300 °C, so the SiC、C double layer structure is formed. However, due to the lack of silicon sources, SiC can only exist as thin layers [52,53]. Furthermore, such encapsulated structure can not only effectively protect the metal particles against corrosion in a harsh environment, but also increase the interface layer between materials, so that materials can produce more interface polarization under the action of microwave, and improve the absorption capacity of materials to microwave [54,55]. HRTEM images show that the periodic lattice fringes with good resolution are about 0.18 nm, 0.25 nm, and 0.35 nm, corresponding to the crystal planes of Ni (002), SiC (111), and C (002), respectively. In Figure 5c we can see that the surface C layer is bent into a discontinuous sheet, defects will naturally occur at these positions, and a large number of dipoles are easily gathered at the defects, which is conducive to the dipole polarization effect of the absorber, which may lead to electromagnetic waves loss. The high-angle annular dark-field scanning TEM (HAADF-STEM) image and elemental mappings disclose the uniform distribution of C, Ni, and Si throughout the fibrous nanohybrids. It can be seen from Figures S3 and S4 that no nano-structure is generated on the surface of NC and SC catalysts. Ni nanoparticles of NC catalyst are uniformly anchored on the surface of carbon nanofibers, while the SC surface is rough and no nano-structure can be seen from SEM. However, many fine SiC grains were found on the surface and the fibers showed a core-shell structure. There are many interfaces between different catalyst structures. Under the action of a microwave, the electrons move and gather at the interface, which makes it easy to generate interface polarization and improve microwave absorption capacity [43].

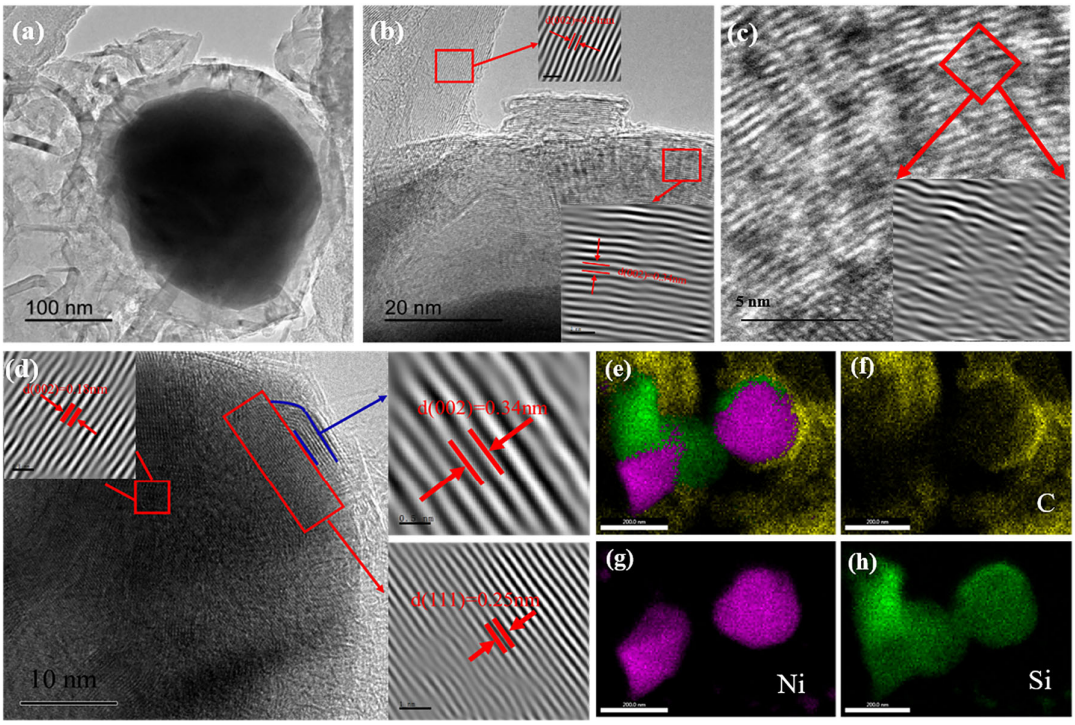

Figure 5. (a-b) TEM images of NSC catalyst; (c-d) HRTEM image.

 doi:10.20944/preprints202407.0347.v1

3.2. Microwave-induced catalytic degradation of MB

Figure 6 shows the degradation curves of different catalytic materials for MW catalytic oxidation of methylene blue at a given power in a MW (450 W, 2450 MHz). Before microwave-assisted degradation of methylene blue, we first soaked these samples with methylene blue solution in the dark for 30 minutes to achieve adsorption equilibrium. Samples are taken every 30 seconds until either of the two visually visible samples fades and the test is stopped. 664 nm is the absorption peak of the MB chromophore and the parent ring structure, so its degradation rate can be determined by the maximum absorption wavelength of 664 nm. By comparing the absorption peaks of the three catalysts at 664 nm, the UV-vis spectra of NSC, SC, and NC catalysts are shown in Figure S5. It can be found that with the increase of time, the absorption peaks of the NSC catalyst at 664 nm decreased significantly, while the absorption peaks of NC and SC to MB decreased slowly. Figure 6(a) shows the time-degradation rates of different catalysts. It can be seen from the figure that the NSC catalyst almost completely degrades after 90s, with a degradation rate close to 100%, while the degradation rates of SC and NC are about 45% and 19%, respectively. The results showed that the microwave-assisted degradation of methylene blue by NSC catalyst was the best. The degradation kinetics results of MB in the 90s are shown in Figure 6(b), which indicates that the degradation kinetics of MB in the 90s by the three catalysts under microwave conditions basically belong to first-order reaction kinetics. The microwave-induced degradation rate constants of MB of different catalysts are shown in Figure 6(c). The reaction rates k of NSC, SC, and NC are 0.1951, 0.0100, and 0.0051, respectively. In other words, the degradation rate of MB by NSC is about 19.51 times that of SC and 38.25 times that of NC. By comparing SC and NC samples, the degradation efficiency of the SC system is higher than that of NC. It is also confirmed that the presence of SiC in the ternary NSC catalyst contributes more to degradation than Ni. The above experimental results show that NSC has better MW catalytic activity and higher MB degradation catalytic activity compared with the other two catalysts.

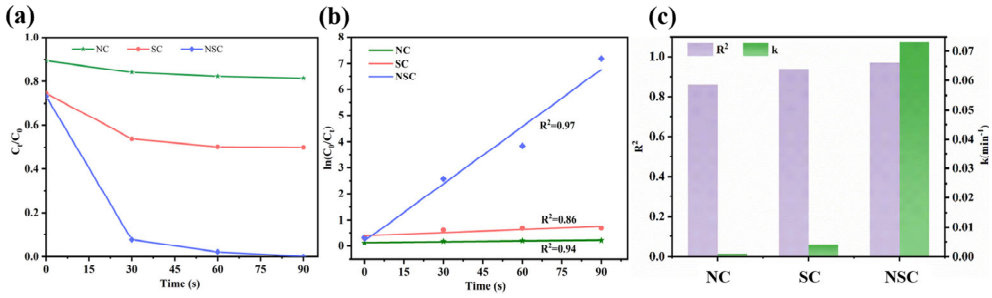

Figure 6. (a) Degradation curves of MB by different catalysts under microwave irradiation; (b) the corresponding degradation rate curve; (c) corresponding degradation slope and R^2 of composites under microwave catalysis.

3.3. Electromagnetic wave absorption characteristics and catalytic degradation mechanism of NSC composite materials

To explore the reason why the NSC catalyst has a good degradation efficiency of MB under the action of microwave, we tested the electromagnetic wave absorption performance of the catalyst. Figure 7(a-f) plotted the electromagnetic parameters of the NSC catalyst to study its electromagnetic wave absorption performance. It is generally true that the −10 dB is equivalent to 90% of the total absorbed energy of the EM wave, and the −20 dB is equivalent to 99% of the total energy absorbed by the EM wave [56]. Reflection loss (RL) data about NSC for a frequency range of 2-18 GHz is illustrated by the curves in Figure 7(a). The prepared NSC catalyst exhibits excellent microwave absorption performance, with a maximum reflection loss (RL_{max}) of 51.40 dB at 12.5GHz. the corresponding matching thickness is 1.418 mm, and the effective RL bandwidth (RL > -10 dB) is 11.4-14.1 GHz.

As shown in Figure 7(b), the permittivity (ε'、ε'') of the catalyst decreases gradually with the increase of frequency, which may be related to the polarization and interface relaxation at the interface between Ni, SiC, and C layer. According to the value of $\tan\delta_\varepsilon$ ($\tan\delta_\varepsilon=\varepsilon''/\varepsilon'$), the dielectric loss

 doi:10.20944/preprints202407.0347.v1

capacity is further estimated. Interestingly, tanδ_ε values of NSC catalysts peak at 9GHz and 12.7 GHz, as shown in Figure 7d. The reason is that the dielectric loss ability is affected simultaneously by the polarization effect and the conductive loss [57].

In addition to dielectric loss, magnetic loss also plays an important role. As shown in Figure 7d, the tanδ_μ value of the catalyst shows a similar trend to the imaginary part (μ'') of the permeability, indicating that the magnetic energy dissipation capacity is the key factor of the magnetic loss [58–60]. It is worth noting that in Figure 7(d), the peak of the magnetic loss (tanδ_μ) around 13.8GHz comes from both natural and exchange resonance. It is clearly observed from Figure 7d that the value of tanδ_ε is significantly larger than tanδ_μ. This indicates that dielectric loss is the main contributor to excellent microwave absorption performance.

To further investigate the mechanism of dielectric and magnetic loss, Figure 7(e-f) illustrates the Cole-Cole plots and c_0 curves of the samples. Figure 7(e) shows the Cole-Cole semicircles of the sample, with each semicircle corresponding to debye relaxation [61]. Obviously, there are multiple decomposable semicircles in the ε' and ε'' curves, indicating that the debye relaxation process caused by interfacial polarization and dipole polarization occurs in the samples. In addition, there are almost no straight lines at the ends of the Cole-Cole diagram, indicating that there is almost no conduction loss during the whole process.

The magnetic loss mechanism mainly consists of three parts: exchange resonance, natural resonance, and eddy current loss. In general, the eddy current losses of absorbing materials can be described by the value of c_0($c_0=\mu''(\mu')^{-2}f^{-1}$). When the value of c_0 is constant with increasing frequency, eddy current loss is dominant in magnetic loss. If c_0 changes with f, eddy current losses are suppressed, and natural resonance and exchange resonance are the main sources of magnetic losses [62]. As shown in Figure 7f, the c_0 curve of the sample fluctuates significantly at the frequency of 2-18 GHz, indicating that exchange resonance and natural resonance play a crucial role in the magnetic loss of the catalyst.

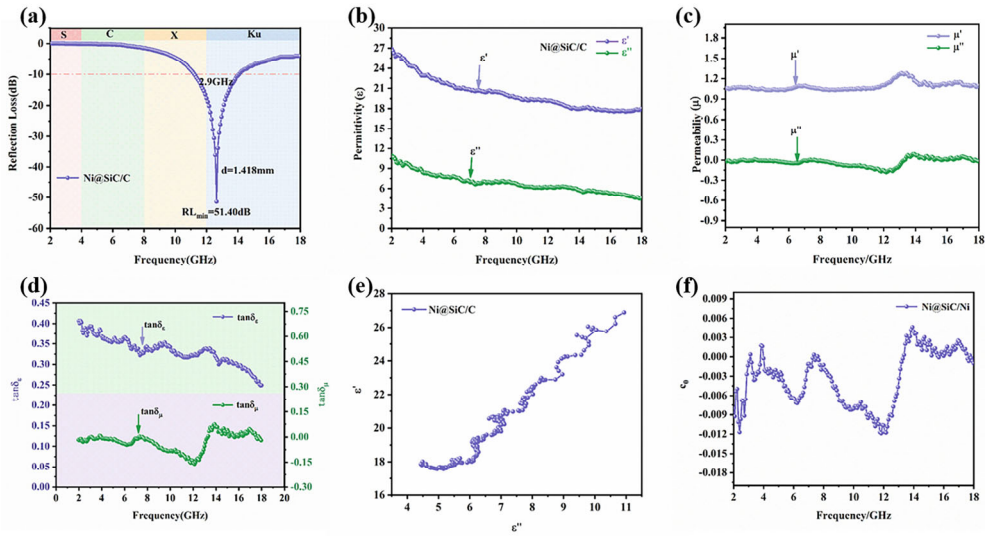

Figure 7. (a) RL curves at a thickness of 1.418 mm; (b) Real/ imaginary permittivity of NSC; (c) Real/ imaginary permeability of NSC; (d) Frequency dependence of dielectric loss and magnetic loss of sample; (e) Typical Cole-Cole semicircles (ε'' versus ε') for NSC; (f) c_0 values of NSC.

Based on the above analysis, the mechanism of degradation of methylene blue by NSC catalyst under microwave irradiation was further studied and summarized the efficient degradation rate of MB by binuclear NSC catalyst composed of C, Ni, and SiC is mainly attributed to the following points. (1) The prepared catalyst has excellent microwave absorption characteristics, which ensures that MB can fully absorb microwave energy and convert it into heat energy in the process of microwave degradation. (2) SiC as a polar molecule, under microwave irradiation, will produce dipole

 doi:10.20944/preprints202407.0347.v1

polarization. In addition, there are a small number of defects in the catalyst, where the electron aggregation occurs dipole polarization. (3) There are abundant phase boundaries in the composites, which can cause more interfacial polarization and multiple relaxation. The polarization mechanism occurring in processes (2) and (3) will cause the material to generate a lot of heat, making electrons in an active and unstable state, and the transition will generate hole electron pairs. At the same time, one-dimensional carbon nanotubes can provide more conductive paths to facilitate the transport of excited hopping electrons. These hole pairs react with O_2 and H_2O in water to form various active substances such as •OH, O_2^- and H^+ active groups. (4) Due to the characteristics of microwave selective heating, the absorption capacity of each material in the composite is different, which leads to the temperature gradient of the catalyst, resulting in many "hot spots". The "hot spot" reacts with water to form active groups such as •H and •OH. (5) A unique discharge phenomenon will be produced when the metal is irradiated by microwave. The discharge process will be accompanied by the release of plasma, which not only can shape local high temperatures to strengthen microwave heating, but also can generate plasma which can significantly promote chemical reaction, which can generate •OH, O_2^- and H^+ active groups. Under the action of microwave, it is the synergistic effect between various elements that makes the degradation of MB (methylene blue) easier to occur.

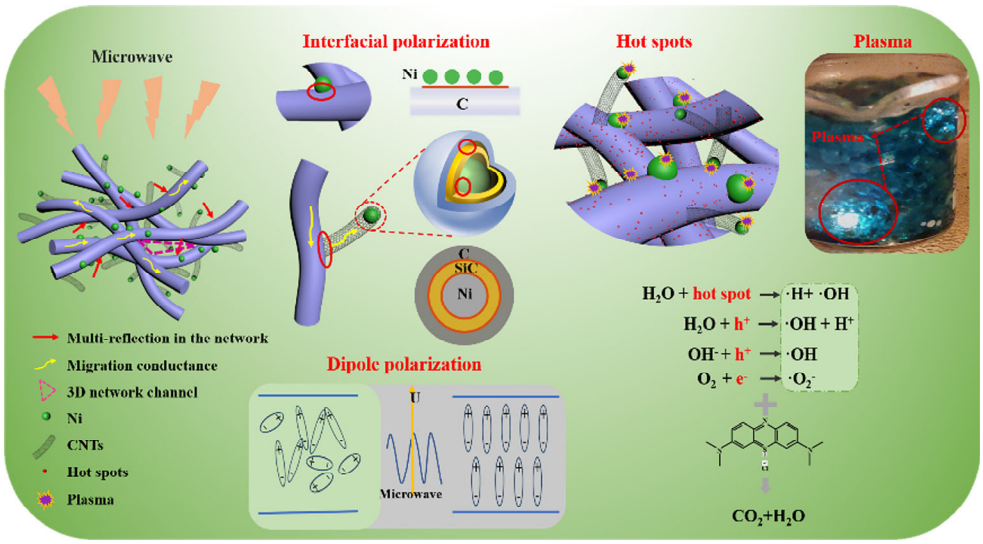

Figure 8. Degradation mechanism of Ni@SiC/CNFs composites under microwave irradiation.

4. Conclusions

In this study, catalysts with different structures were successfully prepared by adjusting the raw materials in precursor solution by electrostatic spinning method and used for the degradation of high concentration MB solution under microwave irradiation. The characterization results of different catalysts suggest that the microstructure of materials plays an important role in the degradation rate of MB. Under the action of microwave, the NSC catalyst showed excellent catalytic activity, and MB degradation in 1.5 minutes. Compared with NC and SC, the reaction rates were 38.25 and 19.51 times higher, which was mainly attributed to the synergistic effect of the thermal effect, non-thermal effect, and plasma effect of the NSC catalyst under the action of microwave. Under these effects, a large number of active radicals •OH, H^+, and O_2^- were produced, and these active radicals could rapidly oxidize methylene blue dye. So that it is rapidly degraded into non-toxic and harmless small molecules. It is expected that Ni@SiC/CNFs with high microwave-assisted catalytic activity will greatly promote its practical application in the removal of organic pollutants.

Supplementary Materials: The following supporting information can be downloaded at the website of this paper posted on Preprints.org., Figure S1: title; Table S1: title; Video S1: title.

Author Contributions: Conceptualization, H.O., and J.L.; validation, J.L, and L.B.; formal analysis, T.S., and Y.L.; writing—original draft preparation, J.L.; writing—review and editing, C.L. All authors have read and agreed to the published version of the manuscript.

Funding: This research was supported by the National Nature Science Foundation of China (Grant No. 52173299, 52372087).

Data Availability Statement: Not applicable.

Acknowledgments: The authors would like to thank Jinfan Liu for his help in experimental section.

Conflicts of Interest: The authors declare no conflict of interest.

References

1. Nasir, A.M.; Awang, N.; Jaafar, J.; Ismail, A.F.; Othman, M.H.D.; A. Rahman, M.; Aziz, F.; Mat Yajid, M.A. Recent progress on fabrication and application of electrospun nanofibrous photocatalytic membranes for wastewater treatment: A review. *Journal of Water Process Engineering* **2021**, *40*, doi:10.1016/j.jwpe.2020.101878.
2. Xia, H.; Li, C.; Yang, G.; Shi, Z.; Jin, C.; He, W.; Xu, J.; Li, G. A review of microwave-assisted advanced oxidation processes for wastewater treatment. *Chemosphere* **2022**, *287*, doi:10.1016/j.chemosphere.2021.131981.
3. Liu, Z.; Zhang, W.; Liang, Q.; Huang, J.; Shao, B.; Liu, Y.; Liu, Y.; He, Q.; Wu, T.; Gong, J.; et al. Microwave-assisted high-efficiency degradation of methyl orange by using $CuFe_2O_4$/CNT catalysts and insight into degradation mechanism. *Environ Sci Pollut Res Int* **2021**, *28*, 42683-42693, doi:10.1007/s11356-021-13694-z.
4. Khoshnam, M.; Farahbakhsh, J.; Zargar, M.; Mohammad, A.W.; Benamor, A.; Ang, W.L.; Mahmoudi, E. alpha-Fe_2O_3/graphene oxide powder and thin film nanocomposites as peculiar photocatalysts for dye removal from wastewater. *Sci Rep* **2021**, *11*, 20378, doi:10.1038/s41598-021-99849-x.
5. Zhang, Y.; Su, P.; Weathersby, D.; Zhang, Q.; Zheng, J.; Fan, R.; Zhang, J.; Dai, Q. Synthesis of γ-Fe_2O_3-ZnO-biochar nanocomposites for Rhodamine B removal. *Applied Surface Science* **2020**, *501*, doi:10.1016/j.apsusc.2019.144217.
6. Wong, S.; Ghafar, N.A.; Ngadi, N.; Razmi, F.A.; Inuwa, I.M.; Mat, R.; Amin, N.A.S. Effective removal of anionic textile dyes using adsorbent synthesized from coffee waste. *Sci Rep* **2020**, *10*, 2928, doi:10.1038/s41598-020-60021-6.
7. Liu, Y.; Song, L.; Du, L.; Gao, P.; Liang, N.; Wu, S.; Minami, T.; Zang, L.; Yu, C.; Xu, X. Preparation of Polyaniline/Emulsion Microsphere Composite for Efficient Adsorption of Organic Dyes. *Polymers (Basel)* **2020**, *12*, doi:10.3390/polym12010167.
8. Chen, B.; Long, F.; Chen, S.; Cao, Y.; Pan, X. Magnetic chitosan biopolymer as a versatile adsorbent for simultaneous and synergistic removal of different sorts of dyestuffs from simulated wastewater. *Chemical Engineering Journal* **2020**, *385*, doi:10.1016/j.cej.2019.123926.
9. Xue, C.; Mao, Y.; Wang, W.; Song, Z.; Zhao, X.; Sun, J.; Wang, Y. Current status of applying microwave-associated catalysis for the degradation of organics in aqueous phase - A review. *J Environ Sci (China)* **2019**, *81*, 119-135, doi:10.1016/j.jes.2019.01.019.
10. Kubra, K.T.; Salman, M.S.; Hasan, M.N. Enhanced toxic dye removal from wastewater using biodegradable polymeric natural adsorbent. *Journal of Molecular Liquids* **2021**, *328*, doi:10.1016/j.molliq.2021.115468.
11. Gągol, M.; Przyjazny, A.; Boczkaj, G. Wastewater treatment by means of advanced oxidation processes based on cavitation – A review. *Chemical Engineering Journal* **2018**, *338*, 599-627, doi:10.1016/j.cej.2018.01.049.
12. Tian, K.; Hu, L.; Li, L.; Zheng, Q.; Xin, Y.; Zhang, G. Recent advances in persulfate-based advanced oxidation processes for organic wastewater treatment. *Chinese Chemical Letters* **2022**, *33*, 4461-4477, doi:10.1016/j.cclet.2021.12.042.
13. Liang, C.; Niu, H.-Y.; Guo, H.; Niu, C.-G.; Yang, Y.-Y.; Liu, H.-Y.; Tang, W.-W.; Feng, H.-P. Efficient photocatalytic nitrogen fixation to ammonia over bismuth monoxide quantum dots-modified defective ultrathin graphitic carbon nitride. *Chemical Engineering Journal* **2021**, *406*, doi:10.1016/j.cej.2020.126868.
14. Peng, Y.; Li, Y.; Liu, L.; Hao, X.; Cai, K.; Xiong, J.; Hong, W.; Tao, J. New optimization approach for amphoteric/magnetic ramie biosorbent in dyestuff adsorption. *Biochemical Engineering Journal* **2022**, *181*, doi:10.1016/j.bej.2022.108379.

15. Wang, H.; Zhao, Z.; Zhang, X.; Dong, W.; Cao, Z.; He, L.; Wang, X. Rapid decomplexation of Ni-EDTA by microwave-assisted Fenton reaction. *Chemical Engineering Journal* **2020**, *381*, doi:10.1016/j.cej.2019.122703.
16. Garcia-Costa, A.L.; Zazo, J.A.; Casas, J.A. Microwave-assisted catalytic wet peroxide oxidation: Energy optimization. *Separation and Purification Technology* **2019**, *215*, 62-69, doi:10.1016/j.seppur.2019.01.006.
17. Qi, Y.; Mei, Y.; Li, J.; Yao, T.; Yang, Y.; Jia, W.; Tong, X.; Wu, J.; Xin, B. Highly efficient microwave-assisted Fenton degradation of metacycline using pine-needle-like $CuCo_2O_4$ nanocatalyst. *Chemical Engineering Journal* **2019**, *373*, 1158-1167, doi:10.1016/j.cej.2019.05.097.
18. Hu, L.; Wang, P.; Liu, G.; Zheng, Q.; Zhang, G. Catalytic degradation of p-nitrophenol by magnetically recoverable Fe_3O_4 as a persulfate activator under microwave irradiation. *Chemosphere* **2020**, *240*, 124977, doi:10.1016/j.chemosphere.2019.124977.
19. Garcia-Costa, A.L.; Zazo, J.A.; Rodriguez, J.J.; Casas, J.A. Microwave-assisted catalytic wet peroxide oxidation. Comparison of Fe catalysts supported on activated carbon and γ-alumina. *Applied Catalysis B: Environmental* **2017**, *218*, 637-642, doi:10.1016/j.apcatb.2017.06.058.
20. Lei, Y.; Lin, X.; Liao, H. New insights on microwave induced rapid degradation of methyl orange based on the joint reaction with acceleration effect between electron hopping and Fe^{2+}-H_2O_2 reaction of $NiFeMnO_4$ nanocomposites. *Separation and Purification Technology* **2018**, *192*, 220-229, doi:10.1016/j.seppur.2017.09.067.
21. Shen, M.; Fu, L.; Tang, J.; Liu, M.; Song, Y.; Tian, F.; Zhao, Z.; Zhang, Z.; Dionysiou, D.D. Microwave hydrothermal-assisted preparation of novel spinel-$NiFe_2O_4$/natural mineral composites as microwave catalysts for degradation of aquatic organic pollutants. *J Hazard Mater* **2018**, *350*, 1-9, doi:10.1016/j.jhazmat.2018.02.014.
22. Qian, C.; Dai, J.; Tian, Y.; Duan, Y.; Li, Y. Efficient degradation of Fipronil in water by microwave-induced argon plasma: Mechanism and degradation pathways. *Sci Total Environ* **2020**, *725*, 138487, doi:10.1016/j.scitotenv.2020.138487.
23. Zhao, C.; Xue, L.; Zhou, Y.; Zhang, Y.; Huang, K. A microwave atmospheric plasma strategy for fast and efficient degradation of aqueous p-nitrophenol. *J Hazard Mater* **2021**, *409*, 124473, doi:10.1016/j.jhazmat.2020.124473.
24. Xu, G.; Jiang, H.; Stapelberg, M.; Zhou, J.; Liu, M.; Li, Q.J.; Cao, Y.; Gao, R.; Cai, M.; Qiao, J.; et al. Self-Perpetuating Carbon Foam Microwave Plasma Conversion of Hydrocarbon Wastes into Useful Fuels and Chemicals. *Environ Sci Technol* **2021**, *55*, 6239-6247, doi:10.1021/acs.est.0c06977.
25. Zhang, P.; Liang, C.; Wu, M.; Chen, X.; Liu, D.; Ma, J. High-efficient microwave plasma discharging initiated conversion of waste plastics into hydrogen and carbon nanotubes. *Energy Conversion and Management* **2022**, *268*, doi:10.1016/j.enconman.2022.116017.
26. Pang, Y.; Lei, H. Degradation of p-nitrophenol through microwave-assisted heterogeneous activation of peroxymonosulfate by manganese ferrite. *Chemical Engineering Journal* **2016**, *287*, 585-592, doi:10.1016/j.cej.2015.11.076.
27. Zhou, J.; You, Z.; Xu, W.; Su, Z.; Qiu, Y.; Gao, L.; Yin, C.; Lan, L. Microwave irradiation directly excites semiconductor catalyst to produce electric current or electron-holes pairs. *Sci Rep* **2019**, *9*, 5470, doi:10.1038/s41598-019-41002-w.
28. Pawar, S.P.; Gandi, M.; Bose, S. High performance electromagnetic wave absorbers derived from PC/SAN blends containing multiwall carbon nanotubes and Fe_3O_4 decorated onto graphene oxide sheets. *RSC Advances* **2016**, *6*, 37633-37645, doi:10.1039/c5ra25435c.
29. Menéndez, J.A.; Arenillas, A.; Fidalgo, B.; Fernández, Y.; Zubizarreta, L.; Calvo, E.G.; Bermúdez, J.M. Microwave heating processes involving carbon materials. *Fuel Processing Technology* **2010**, *91*, 1-8, doi:10.1016/j.fuproc.2009.08.021.
30. Li, C.; Xia, H.; Zhang, L.; Wang, S.; Peng, J.; Cheng, S.; Shu, J.; Jiang, X.; Zhang, Q. Analysis of dielectric characterization and microwave adsorbing properties in organism-contained spent carbon: An efficient regeneration method via microwave-assisted ultrasound. *Chemical Engineering and Processing - Process Intensification* **2018**, *125*, 74-86, doi:10.1016/j.cep.2018.01.007.
31. Yuan, X.; Wang, R.; Huang, W.; Kong, L.; Guo, S.; Cheng, L. Morphology Design of Co-electrospinning MnO-VN/C Nanofibers for Enhancing the Microwave Absorption Performances. *ACS Appl Mater Interfaces* **2020**, *12*, 13208-13216, doi:10.1021/acsami.9b23310.
32. Chen, C.; Xi, J.; Zhou, E.; Peng, L.; Chen, Z.; Gao, C. Porous Graphene Microflowers for High-Performance Microwave Absorption. *Nanomicro Lett* **2018**, *10*, 26, doi:10.1007/s40820-017-0179-8.

33. Li, J.; Zhang, F.; Lu, H.; Guo, W.; He, X.; Yuan, Y. Heterogeneous rod-like Ni@C composites toward strong and stable microwave absorption performance. *Carbon* **2021**, *181*, 358-369, doi:10.1016/j.carbon.2021.05.031.
34. Wang, B.; Wu, Q.; Fu, Y.; Liu, T. A review on carbon/magnetic metal composites for microwave absorption. *Journal of Materials Science & Technology* **2021**, *86*, 91-109, doi:10.1016/j.jmst.2020.12.078.
35. Hidaka, H.; Saitou, A.; Honjou, H.; Hosoda, K.; Moriya, M.; Serpone, N. Microwave-assisted dechlorination of polychlorobenzenes by hypophosphite anions in aqueous alkaline media in the presence of Pd-loaded active carbon. *J Hazard Mater* **2007**, *148*, 22-28, doi:10.1016/j.jhazmat.2007.01.143.
36. Sun, G.; Dong, B.; Cao, M.; Wei, B.; Hu, C. Hierarchical Dendrite-Like Magnetic Materials of Fe_3O_4, γ-Fe_2O_3, and Fe with High Performance of Microwave Absorption. *Chemistry of Materials* **2011**, *23*, 1587-1593, doi:10.1021/cm103441u.
37. Ren, Y.; Zhu, C.; Zhang, S.; Li, C.; Chen, Y.; Gao, P.; Yang, P.; Ouyang, Q. Three-dimensional SiO_2@Fe_3O_4 core/shell nanorod array/graphene architecture: synthesis and electromagnetic absorption properties. *Nanoscale* **2013**, *5*, 12296-12303, doi:10.1039/c3nr04058e.
38. Singh, S.; Bhaskar, R.; Narayanan, K.B.; Kumar, A.; Debnath, K. Development of silicon carbide (SiC)-based composites as microwave-absorbing materials (MAMs): A review. *Journal of the European Ceramic Society* **2024**, *44*, 7411-7431, doi:10.1016/j.jeurceramsoc.2024.05.032.
39. Singh, S.; Maurya, A.K.; Gupta, R.; Kumar, A.; Singh, D. Improved microwave absorption behavioral response of Ni/SiC and Ni/SiC/graphene composites: A comparative insight. *Journal of Alloys and Compounds* **2020**, *823*, doi:10.1016/j.jallcom.2020.153780.
40. Wang, Y.; Di, X.; Chen, J.; She, L.; Pan, H.; Zhao, B.; Che, R. Multi-dimensional C@NiCo-LDHs@Ni aerogel: Structural and componential engineering towards efficient microwave absorption, anti-corrosion and thermal-insulation. *Carbon* **2022**, *191*, 625-635, doi:10.1016/j.carbon.2022.02.016.
41. Hu, P.; Dong, S.; Li, X.; Chen, J.; Hu, P. Flower-like $NiCo_2S_4$ Microspheres Based on Nanosheet Self-Assembly Anchored on 3D Biomass-Derived Carbon for Efficient Microwave Absorption. *ACS Sustainable Chemistry & Engineering* **2020**, *8*, 10230-10241, doi:10.1021/acssuschemeng.0c03013.
42. Liu, L.; Yang, S.; Hu, H.; Zhang, T.; Yuan, Y.; Li, Y.; He, X. Lightweight and Efficient Microwave-Absorbing Materials Based on Loofah-Sponge-Derived Hierarchically Porous Carbons. *ACS Sustainable Chemistry & Engineering* **2018**, *7*, 1228-1238, doi:10.1021/acssuschemeng.8b04907.
43. Li, H.; Gao, S.; Tong, H.; Liu, Y.; Wu, A.; Hao, H. The capacitive loss of microwave energy in Ni@SiC@C core/bi-shell nanoparticles. *Chemical Engineering Journal* **2022**, *434*, doi:10.1016/j.cej.2022.134655.
44. Candace K. Chan, R.N.P., Michael J. O'Connell, Brian A. Korgel, and Yi Cui. Solution-Grown Silicon Nanowires for Lithium-Ion Battery Anodes. *ACS Nano* **2010**, *4*, 1443–1450.
45. Liu, Y.; Liu, Y.; Choi, W.C.; Chae, S.; Lee, J.; Kim, B.-S.; Park, M.; Kim, H.Y. Highly flexible, erosion resistant and nitrogen doped hollow SiC fibrous mats for high temperature thermal insulators. *Journal of Materials Chemistry A* **2017**, *5*, 2664-2672, doi:10.1039/c6ta09475a.
46. Wang, B.; Wang, Y.; Lei, Y.; Wu, N.; Gou, Y.; Han, C.; Fang, D. Hierarchically porous SiC ultrathin fibers mat with enhanced mass transport, amphipathic property and high-temperature erosion resistance. *J. Mater. Chem. A* **2014**, *2*, 20873-20881, doi:10.1039/c4ta04847d.
47. Huo, Y.; Tan, Y.; Zhao, K.; Lu, Z.; Zhong, L.; Tang, Y. Enhanced electromagnetic wave absorption properties of Ni magnetic coating-functionalized SiC/C nanofibers synthesized by electrospinning and magnetron sputtering technology. *Chemical Physics Letters* **2021**, *763*, doi:10.1016/j.cplett.2020.138230.
48. Li, T.; Luo, G.; Liu, K.; Li, X.; Sun, D.; Xu, L.; Li, Y.; Tang, Y. Encapsulation of Ni_3Fe Nanoparticles in N-Doped Carbon Nanotube–Grafted Carbon Nanofibers as High-Efficiency Hydrogen Evolution Electrocatalysts. *Advanced Functional Materials* **2018**, *28*, doi:10.1002/adfm.201805828.
49. Liu, S.; Wang, Z.; Zhou, S.; Yu, F.; Yu, M.; Chiang, C.Y.; Zhou, W.; Zhao, J.; Qiu, J. Metal-Organic-Framework-Derived Hybrid Carbon Nanocages as a Bifunctional Electrocatalyst for Oxygen Reduction and Evolution. *Adv Mater* **2017**, *29*, doi:10.1002/adma.201700874.
50. Wu, R.; Wang, D.P.; Rui, X.; Liu, B.; Zhou, K.; Law, A.W.; Yan, Q.; Wei, J.; Chen, Z. In-situ formation of hollow hybrids composed of cobalt sulfides embedded within porous carbon polyhedra/carbon nanotubes for high-performance lithium-ion batteries. *Adv Mater* **2015**, *27*, 3038-3044, doi:10.1002/adma.201500783.
51. Tang, J.; Salunkhe, R.R.; Liu, J.; Torad, N.L.; Imura, M.; Furukawa, S.; Yamauchi, Y. Thermal conversion of core-shell metal-organic frameworks: a new method for selectively functionalized nanoporous hybrid carbon. *J Am Chem Soc* **2015**, *137*, 1572-1580, doi:10.1021/ja511539a.

52. Li, D.; Liao, H.; Kikuchi, H.; Liu, T. Microporous Co@C Nanoparticles Prepared by Dealloying CoAl@C Precursors: Achieving Strong Wideband Microwave Absorption via Controlling Carbon Shell Thickness. *ACS Appl Mater Interfaces* **2017**, *9*, 44704-44714, doi:10.1021/acsami.7b13538.
53. Huang, F.; Fan, S.; Li, X.; Qu, X.; Tian, Y.; Zhang, X.; Zhang, Z.; Dong, X.; Cao, T. Enhanced dielectric and conductivity properties of carbon-coated SiC nanocomposites in the terahertz frequency range. *Nanotechnology* **2021**, *32*, 265705, doi:10.1088/1361-6528/abf070.
54. Deng, J.; Ren, P.; Deng, D.; Yu, L.; Yang, F.; Bao, X. Highly active and durable non-precious-metal catalysts encapsulated in carbon nanotubes for hydrogen evolution reaction. *Energy Environ. Sci.* **2014**, *7*, 1919-1923, doi:10.1039/c4ee00370e.
55. Cui, X.; Ren, P.; Deng, D.; Deng, J.; Bao, X. Single layer graphene encapsulating non-precious metals as high-performance electrocatalysts for water oxidation. *Energy & Environmental Science* **2016**, *9*, 123-129, doi:10.1039/c5ee03316k.
56. Cai, Z.; Su, L.; Wang, H.; Xie, Q.; Gao, H.; Niu, M.; Lu, D. Hierarchically assembled carbon microtube@SiC nanowire/Ni nanoparticle aerogel for highly efficient electromagnetic wave absorption and multifunction. *Carbon* **2022**, *191*, 227-235, doi:10.1016/j.carbon.2022.01.036.
57. Di, X.; Wang, Y.; Lu, Z.; Cheng, R.; Yang, L.; Wu, X. Heterostructure design of Ni/C/porous carbon nanosheet composite for enhancing the electromagnetic wave absorption. *Carbon* **2021**, *179*, 566-578, doi:10.1016/j.carbon.2021.04.050.
58. Li, D.; Guo, K.; Wang, F.; Wu, Z.; Zhong, B.; Zuo, S.; Tang, J.; Feng, J.; Zhuo, R.; Yan, D.; et al. Enhanced microwave absorption properties in C band of Ni/C porous nanofibers prepared by electrospinning. *Journal of Alloys and Compounds* **2019**, *800*, 294-304, doi:10.1016/j.jallcom.2019.05.284.
59. Ye, X.; Zhang, J.; Chen, Z.; Xiang, J.; Jiang, Y.; Xie, F.; Ma, X. Microwave absorption properties of Ni/C@SiC composites prepared by precursor impregnation and pyrolysis processes. *Defence Technology* **2023**, *21*, 94-102, doi:10.1016/j.dt.2021.11.005.
60. Wu, F.; Liu, Z.; Wang, J.; Shah, T.; Liu, P.; Zhang, Q.; Zhang, B. Template-free self-assembly of MXene and CoNi-bimetal MOF into intertwined one-dimensional heterostructure and its microwave absorbing properties. *Chemical Engineering Journal* **2021**, *422*, doi:10.1016/j.cej.2021.130591.
61. Huang, B.; Wang, Z.; Hu, H.; Xiu, Z.; Huang, X.; Yue, J.; Wang, Y. Enhancement of the microwave absorption properties of PyC-SiCf/SiC composites by electrophoretic deposition of SiC nanowires on SiC fibers. *Ceramics International* **2020**, *46*, 9303-9310, doi:10.1016/j.ceramint.2019.12.185.
62. Li, W.; Guo, F.; Wei, X.; Du, Y.; Chen, Y. Preparation of Ni/C porous fibers derived from jute fibers for high-performance microwave absorption. *RSC Adv* **2020**, *10*, 36644-36653, doi:10.1039/d0ra06817a.